Nanoscale Dynamics, Stochastic Modeling, and Multivariable Control of a Planar Magnetic Levitator

Won-jong Kim

Abstract: This paper presents a high-precision magnetically levitated (maglev) stage to meet demanding motion specifications in the next-generation precision manufacturing and nanotechnology. Characterization of dynamic behaviors of such a motion stage is a crucial task. In this paper, we address the issues related to the stochastic modeling of the stage including transfer function identification, and noise/disturbance analysis and prediction. Provided are test results on precision dynamics, such as fine settling, effect of optical table oscillation, and position ripple. To deal with the dynamic coupling in the platen, we designed and implemented a multivariable linear quadratic regulator, and performed time-optimal control. We demonstrated how the performance of the current maglev stage can be improved with these analyses and experimental results. The maglev stage operates with positioning noise of 5 nm rms in x and y, acceleration capabilities in excess of $2g(20\ \mathrm{m/s^2})$, and closed-loop crossover frequency of 100 Hz.

Keywords: Optimal control applications, system identification and estimation applications, electric motor, modern actuating device, semiconductor manufacturing systems.

1. INTRODUCTION

We have developed a high-precision magnetically levitated (maglev) stage for the next-generation precision manufacturing and nanotechnology. This stage as shown in Fig. 1 is the world's first maglev stage that provides fine six-degree-of-freedom (6-DOF) motion controls, and realizes large planar motions with only a single maglev moving part, namely the platen. This stage is capable of providing all the motions required for a wafer stepper in photolithography in semiconductor manufacturing; the platen is driven in all 6-DOF motions with small adjustments for focusing and alignment and with large planar motions for positioning across the lens field of view. Its current design is optimized to suit for the motion requirement of such an application.

The wafer stepper is operated in step, expose, and repeat sequence to position the wafer under the lens for lithography [1,2]. The die sites on the wafer are exposed by patterned ultraviolet light as defined by the mask. The one-step distance depends on the dimension of the die sites whose typical lateral dimension is on the order of 20 mm. As the time duration for moving the wafer from one die site to another heavily affects the throughput, faster positioning speed is desirable. In steppers, a die site under the lithographic lens is exposed while the wafer is at a standstill. There are also advanced step-and-scan type lithography tools where exposure occurs on the fly. Therefore, precise position control is very important in the current and future deep-submicron lithography technology. We thus have two important control objectives for the levitator as prototype semiconductor manufacturing equipment. (1) Maintain the position the platen as fast as possible in the transition from one die-site to another. Fig. 2 shows the overall control loop of the stage.

Since only the platen generates all required motions in the maglev stage, its dynamics is coupled in

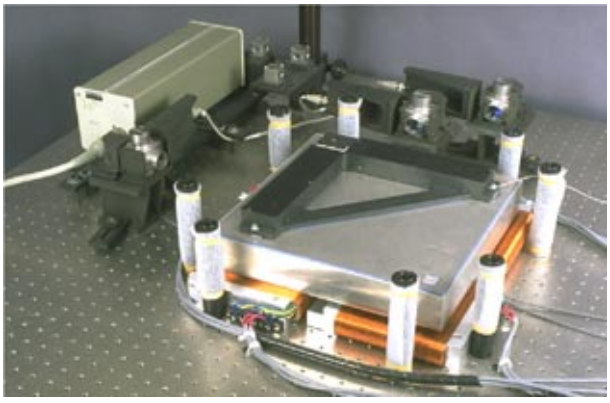

Fig. 1. Photograph of a high-precision planar maglev stage. The horizontal positions are measured at the L-shaped mirror by laser interferometers. The vertical positions are measured at the bottom of the platen by capacitance sensors.

Manuscript received January 10, 2003; accepted March 11, 2003. Recommended by Editor Keum-Shik Hong. This work was supported by the National Science Foundation under grant Nos. DMI-9860697 and CMS-0116642. The author wishes to thank Prof. David L. Trumper at MIT and Mr. James H. Goldie at Foster-Miller, Inc.

Won-jong Kim is with the Department of Mechanical Engineering, Texas A&M University, College Station, TX 77843-3123, U.S.A. (e-mail: wjkim@mengr.tamu.edu).

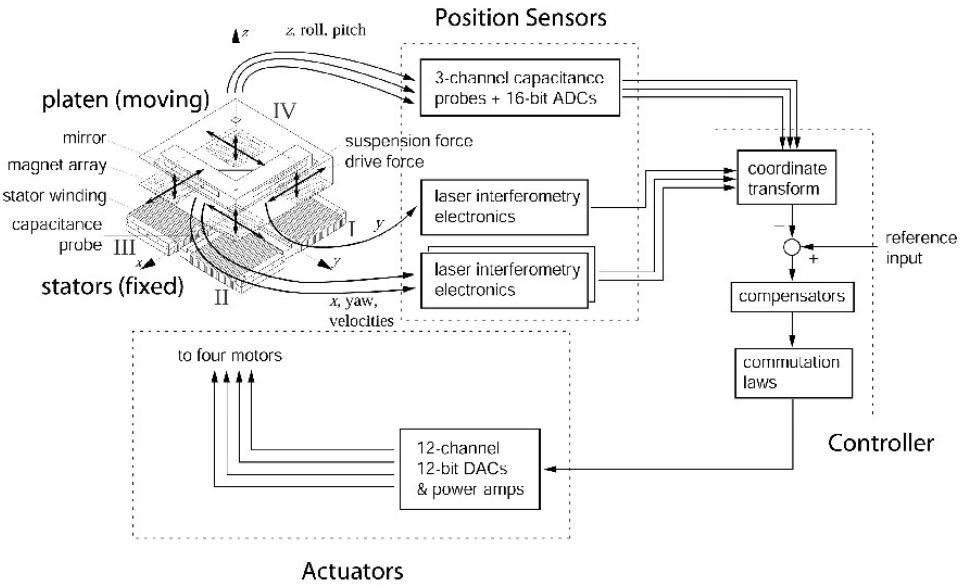

Fig. 2. Overall control loop of the planar magnetic levitator. Three horizontal DOFs are inherently unstable at the equilibrium, and need to be stabilized by active control. The motor forces acting on each magnet array are shown as arrows. Two of motors (I and III) drive the platen in the x-direction, and the other two (II and IV) in the y-direction. The motor forces are coordinated appropriately to control the remaining four degrees of freedom.

six DOFs. Thus, linear multivariable quadratic control is a natural choice to regulate the position of the platen. We designed and implemented a multivariable linear quadratic regulator (LQR) for the lateral modes (x, y and angle around the z-axis) of the maglev stage. Full state feedback was provided by the laser interferometer electronics (HP10897A) for this lateral mode control. To apply the modern multivariable control, a state-space model of the platen dynamics is required. We used the analytical results given in the previous work to derive linearized equations of motion [3].

The time-optimal control is an important motion control problem where a fast response saves time and operational cost. There are many research results on the time-optimal control especially in path planning in robotics [4, 5]. The same economical consideration is also applicable for wafer handling applications in semiconductor manufacturing, since faster movement and settling increases the machine throughput. The time-optimal control problem with actuator saturation was solved and can be found in standard optimal control texts as [6]. We adapt this result and demonstrate that the stage can generate very fast step motions.

In this paper, we report recent developments and test results with the planar magnetic levitator. In the following section, we present a brief overview of the maglev stage. Stochastic transfer function identification and noise analysis and prediction are described in Section 3. In Section 4, we present fine settling performance including effect of optical table oscillation and position ripple. Section 5 presents the multivariable time-optimal control test results. The experimental data presented in Sections 4 and 5 verify the analysis given in Section 3.

2. MAGLEV SYSTEM OVERVIEW

As shown in Fig. 2, the platen is levitated without contact by four novel permanent-magnet linear motors that provide both suspension (vertical) and drive (horizontal) forces [3]. Combinations of the actuator forces, rather than a single motor, generate a translational or rotational motion. With an orthogonal arrangement of the motors as in Fig. 2, the platen generates all 6-DOF motions for focusing and alignment and large two-dimensional step and scanning motions for a high-precision positioner as a wafer stepper stage in semiconductor manufacturing. We allocate three lateral force or torque components to four lateral motor components by the following modal force transformation. For example, we activate positive f_{1x} and f_{3x} in Fig. 2 to get a motion in the positive x-direction. If f_{1x} and f_{3x} are in opposite directions, we get a rotational motion around the z-axis. To generate a positive rotation around the x-axis, we put positive f_{1z} and f_{2z} and negative f_{3z} and f_{4z}. Motions in the three other degrees of freedom are generated in similar ways.

The linear levitation motors consist of Halbach-type magnet arrays [7] attached to the underside of the levitated platen, and coil sets attached to the fixed machine platform. Since all the motor coils are fixed, no

wires need to be connected to the moving part. The platen mass of 5.6 kg is supported against gravity by the combined forces of the four motors. Each motor consumes about 5.4 W to lift the platen. The present design has travel of 50 mm in x and y, travel of 400 μm in z, and is capable of several-milliradian rotations about each of these three orthogonal axes. The maglev stage operates with positioning noise of 5 nm rms in x and y, and demonstrates acceleration capabilities now in excess of 2g (20 m/s^2). The crossover frequency of the control system is 100 Hz, and its phase margin is 53°.

We have three laser axis electronics boards with 0.6-nm position resolution to measure translations and linear velocities along the x- and y-axes and rotations and angular velocities around the z-axis. Three capacitance gap gauging systems provide vertical displacement, and rotational angles around x- and y-axis. The zero point of the capacitance gauging system is set at a 450-μm air gap and its sensing range is large enough that the sensors never saturate when the platen sits on the stators. The resolution of this gauging system is 7.8 nm. Control algorithms are implemented digitally in a 320C40 digital signal processor board. A 100-MHz 80486 PC takes care of user interface, such as monitoring levitator states and command interpretation.

3. SYSTEM AND NOISE MODELING

In this section, we address the stochastic modeling including transfer function identification, and noise/disturbance analysis and prediction of the whole levitation system.

3.1. System transfer function

To obtain fast dynamics through high-bandwidth control, high system structural resonant frequency is required for system stability. A stage with a single-moving part like this planar magnetic levitator has advantages over counterparts with multiple moving parts since its mechanical structure is simple and can be made stiff. We constructed the platen in aluminum honeycomb structure to achieve high stiffness-to-mass ratio [2].

Fig. 3 shows a block diagram to obtain the transfer function of the plant, the levitated platen. We apply a stochastic system identification methodology that uses as random disturbance force input. A detailed treatment of the stochastic modeling is covered in classical texts such as [8]. The random disturbance is generated in software with the "rand()" function in the ANSI C language. Since the maglev system is open-loop unstable, the magnitude of the random disturbance (5.0 N) was chosen after many iterations to excite the plant persistently without losing stability [9].

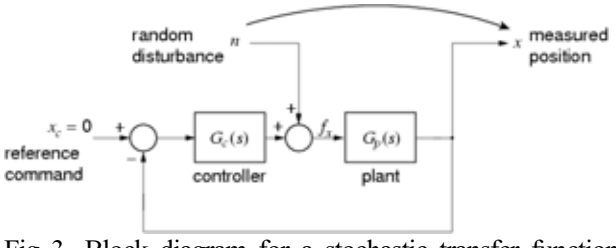

Fig. 3. Block diagram for a stochastic transfer function identification.

The plant transfer function magnitude in x was obtained as presented in Fig. 4. The frequency response of the plant shows a main structural resonance at about 750 Hz with no other significant resonance under that frequency. Comparing with the resonant frequency at 1.2 kHz of the honeycomb sandwich platen only [2], the whole platen shows a lower resonant frequency. This is mainly due to the added masses of the four magnet arrays and the square mirror attached to the platen. This high resonant frequency could be achieved with the planar magnetic levitator because of its simple mechanical structure, its low part count, and the high stiffness-to-mass ratio

3.2. Noise/disturbance modeling and propagation

To determine contributions of each noise source in the maglev system, we use the noise/disturbance propagation model presented in Fig. 5. It shows how noise and disturbance are injected to the closed-loop control system including the controller and the plant. The bandlimited noise V_n modeled as A/D converter quantization and electronic noise enters the control loop as contaminated position measurement. The bandlimited disturbance W_n modeled as floor vibration and D/A converter quantization enters as contaminated input force. In this section, we present the analysis for the vertical motion z.

Since the vertical position is measured by capacitance gauges through A/D converters, we read the sensor and A/D converter noise as position fluctuation. The position error covariance of the A/D converter and electronic noise of the planar magnetic levitator is measured as follows with all analog input terminals electrically short so that there is no stage mechanical movement involved in it.

$$\sigma^2_{A/D\ elec} = 61.2\ \text{nm}^2/(\text{rad/sample}). \qquad (1)$$

The error covariance of the A/D converter quantization can be calculated assuming the real data has a uniform distribution within the quantization interval Δ. For the 16-bit A/D converters we use and with the 500-μm maximum sensing range of the capacitance gauges, Δ is 500 μm/2^{16}. Thus,

$$\sigma^2_{A/D\ quant} = \frac{\Delta^2}{12} = 4.85\ \text{nm}^2/(\text{rad/sample}). \qquad (2)$$

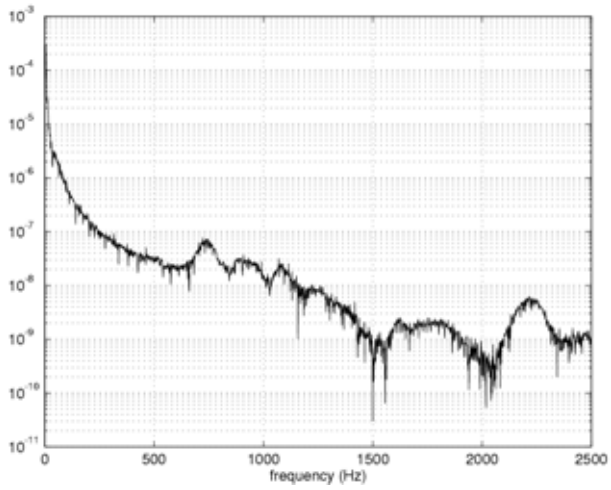

Fig. 4. Measured plant transfer function magnitude in x.

The noises are assumed bandlimited at 800 Hz, the breakpoint frequency of the anti-aliasing filters in front of the A/D converters.

The force error covariance due to D/A quantization can be calculated similarly. Since the full swing of a phase current of the power amplifier is 3 A and the D/A converter is of 12-bit resolution, the current quantization is 3 A/2^{12} = 7.32 × 10^{-4} A. Using the force constant of the levitation motor, 27.7 N/A, and $\Delta = 27.7 \times (7.32 \times 10^{-4})$ N,

$$\sigma^2_{D/A\ quant} = \frac{\Delta^2}{12} = 3.43 \times 10^{-5}\ \mathrm{N}^2/(\mathrm{rad/sample}). \quad (3)$$

The disturbance covariance of the floor vibration-measured on top of the optical table is measured to be 6.65×10^{-3} $\mathrm{N}^2/(\mathrm{rad/sample})$ [10].

Using the error covariances derived above, we can determine the contributions of each noise/disturbance source represented as positioning noise using a Matlab function "covar()." In Fig. 6, the current maglev stage shows a total of 215 nm^2 noise covariance, with all noise/disturbance contributions converted to equivalent continuous spectral densities for fair comparison.

3.3. Noise prediction with better metrology and vibration specifications

In this subsection, we predict the positioning noise in case better metrology and vibration specifications are available. One of the fundamental limitations of the performance of the current planar magnetic levitator is the noise in the capacitance gauge analog electronics. If we could replace the analog capacitance gauge system with laser interferometry with resolution Δ=0.15 nm,

$$\sigma^2_{laser} = \frac{\Delta^2}{12} = 1.88 \times 10^{-3}\ \mathrm{nm}^2/(\mathrm{rad/sample}). \quad (4)$$

This laser interferometry noise covariance replaces $\sigma^2_{A/D\ elec}$ and $\sigma^2_{A/D\ quant}$ altogether of the capacitance gauge system calculated in the previous subsection.

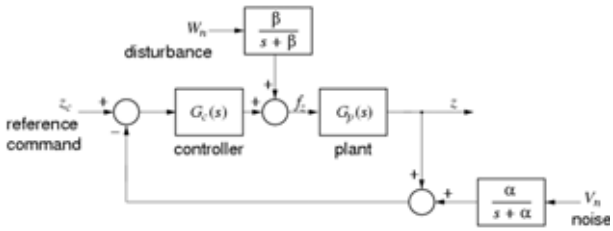

Fig. 5. Stochastic noise/disturbance propagation model.

We see the noise error covariance can be much improved with high-resolution laser interferometry.

On the other hand, the floor vibration contributes significantly to the overall noise covariance. Rejection of seismic floor vibration can be done by active vibration isolation with feedback controllers. In essence, the noise covariance of the current system could be decreased to 1.46 nm^2, which is less than 1% of the current value, if we employed a 0.15-nm resolution laser interferometry instead of the capacitance gauge system, 16-bit instead of 12-bit D/A resolution, and 100 times better effective floor vibration rejection. So, nanometer-order positioning noise for the maglev stage is achievable with adequate metrology and environment control. This noise analysis and prediction is summarized in Fig. 6.

4. PRECISION DYNAMICS

The ultimate goal of the planar magnetic levitator is to position the platen quickly and accurately against disturbance motions and forces, and measurement noise. In this section, observed precision dynamics of the planar magnetic levitator including unmodeled optical table oscillation and its interaction with the levitator dynamics, and position ripple due to nonideality in the levitation motors are presented.

4.1. Fine settling

To demonstrate our stage's motion capability, we accelerate the platen at 1 g(10 $\mathrm{m/s}^2$) until its velocity reaches the maximum slew rate of 200 mm/s of the

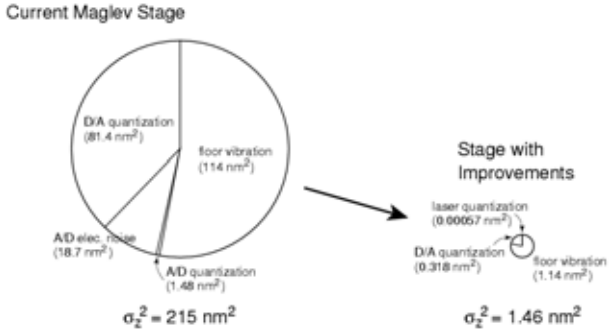

Fig. 6. Noise contributions in the present planar magnetic levitator and their prediction in an improved system with better metrology and vibration specifications.

laser head we use. The platen moves at this constant velocity for 80 ms and is decelerated at 1*g*. This motion trajectory is typically referred to as a trapezoidal velocity profile. So, a 20-mm step command completes in 120 ms. The present lead-lag controllers need roughly 250 ms more to bring the errors in all six axes within their steady-state positioning noise level. This settling time can be reduced by implementing the control design. This can be done by: (1) Move the dominant closed-loop pole more deeply into the left-half *s*-plane by sacrificing phase margin by moving the lag zero to the left in the *s*-plane. (2) Increase the whole closed-loop system bandwidth, which is limited by system structural resonance.

4.2. Optical table oscillation

Fig. 7 shows a 40-mm step response in *x*. The initial and final acceleration of the stage is set at 1/5*g* (2 m/s^2) and the maximum velocity at 200 mm/s. The platen reaches the final positions in 300 ms as commanded. We also present in Fig. 7 the final position error of the same step response on a finer scale. We observe a persistent, low-frequency (about 1.5 Hz), well-damped vibration in the experimental data. This is due to the reaction oscillation of the optical table on which the planar magnetic levitator is mounted after completing the 40-mm step trajectory. This low-frequency oscillation is a genuine problem in any positioning system, whether based on magnetic levitation or an alternative technology, that requires fast responses and high acceleration capabilities. It can be reduced with careful trajectory planning (with an S-shaped velocity profile, for instance) to avoid any abrupt change in acceleration (jerk). Both an enhanced damping at the resonant frequency of the optical table and a high-mass vibration isolator will reduce the magnitude of this oscillation. For a more tight nanometer-order position window, it is recommended to use an active vibration isolation system that reduces the oscillatory motions and rejects the floor vibration at the same time.

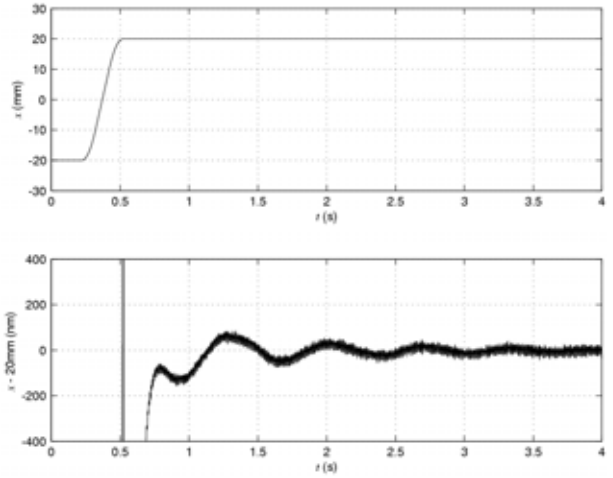

Fig. 7. 40-mm step in *x* (top) and its final position error on a finer scale (bottom) to show the effect of optical table oscillation.

4.3. Position ripple

Only the fundamental magnetic field components are usually taken into consideration to derive motor forces and commutation laws [2]. Since it is impossible to implement perfect sinusoidal magnetic field sources in practice, there will be higher-order force components, so-called force ripple. This force ripple is different from cogging force which is prominent in slotted motors or variable reluctance motors, and is much smaller in magnitude. Similar, but bigger in magnitude, periodic error is also unavoidable in conventional lead screw systems due to the mechanical error of the screw and balls. These error motions can be reduced by open-loop correction. The present maglev system shows ±100-nm order position ripple in z (i.e., the vertical displacement) during a commanded constant-velocity scanning motion at −20-mm/s in the *x*-direction without any correction (Fig. 8). This deterministic error motion due to force ripple can be reduced by feedforward correction [2]. Fig. 8 also shows other axes' dynamic behaviors during the constant-velocity scanning motion for a reference. Reasons for the small position fluctuations in y and ψ (rotation around the *x*-axis) may include fabrication errors, especially the straightness and alignment error of magnet arrays and stator windings. In a point-to-

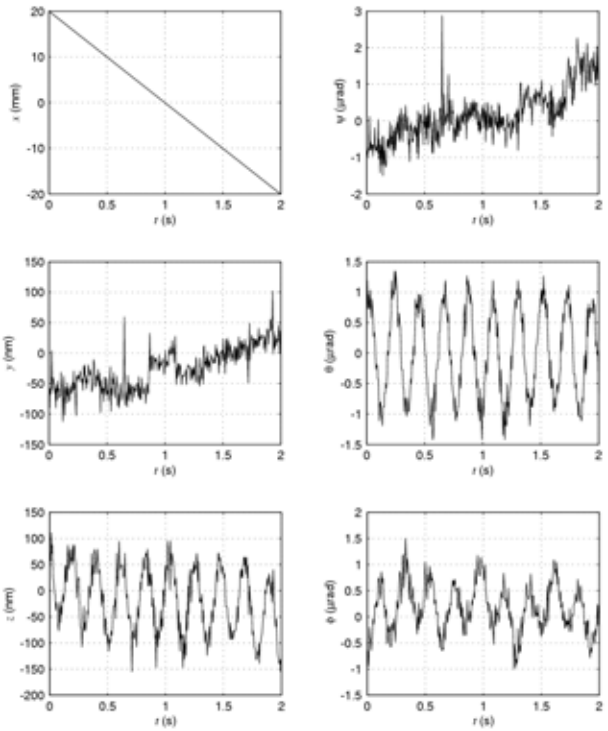

Fig. 8. Position ripple in other 5-DOFs during a 20-mm/s constant-velocity scanning motion in the negative *x*-direction.

point positioning application as in a stepper, this force ripple has an insignificant effect on the overall system performance. There is no such sinusoidal force ripple when the platen moves in the vertical direction since the vertical force depends on an exponential function of z. If the planar maglev stage had 6 phases instead of 3 phases, the ripple force would have been only 2% of the present ripple force [2].

5. MULTIVARIABLE TIME-OPTIMAL CONTROL

Since only the platen generates all required motions, its dynamics is coupled in all six DOFs. In order to understand observed dynamic behaviors and develop high-performance controllers, precise dynamic modeling is required. However, a previous decoupled model does not address dynamic coupling between the axes. Thus, a multivariable linear quadratic controller is a natural choice to regulate the position of the platen. We design a linear quadratic regulator (LQR) for the lateral modes(x, y and angle around the z-axis) of the magnetic levitation stage in this section. We do not need to differentiate position data or build a state estimator for velocity feedback, as full state feedback is provided by the laser interferometer electronics (HP10897A) for the lateral mode control. To apply the multivariable control, a state-space model of the platen dynamics is required. We use the analytical results given in the previous work [3] to derive linearized equations of motion.

The relationship between the force components and the direct-quadrature (dp) current components is shown as [3, 11, 12].

$$\begin{bmatrix} f_y \\ f_z \end{bmatrix} = \frac{1}{2}\mu_0 M_0 \eta_0 N_m G e^{-\gamma_1 z_0} \begin{bmatrix} i_Q \\ i_D \end{bmatrix}. \tag{5}$$

For our levitator, magnet remanence, $\mu_0 M_0 = 1.29$ T; winding turn density, $\eta_0 = 2.49\times10^6$ turns/m^2; effective spatial period $N_m = 15/4$; motor geometric constant $G = 4.90\times10^{-6}$ m^3; pitch $l = 25.6$ mm; and absolute value of fundamental wave number $\gamma_1 = 2\pi/l = 245$ m^{-1}.

The above equations have a nonlinear coupling term of vertical position, z_0 and currents i_Q and i_D. To linearize these force equations, we set the perturbation equations, $z_0 = \bar{z}_0 + \tilde{z}_0$, $i_D = \bar{i}_D + \tilde{i}_D$, and $i_Q = \bar{i}_Q + \tilde{i}_Q$, where $\bar{z}_0$ is the nominal levitation height, which is set 250 μm for the levitator. Ignoring the mass unbalance due to the mirror, the nominal direct-component current $\bar{i}_D$ is calculated 500 mA to levitate the platen. Then, each of four motors generates 14 N as suspension forces, supporting approximately a quarter of the platen weight. The nominal quadrature-component current $\bar{i}_Q$ is zero, as the platen is in dynamic equilibrium and nominal $\bar{f}_y$ is zero.

Let f_1, f_2, f_3 and f_4 be the force vectors acting on four magnet arrays I, II, III, and IV in Fig. 2. Since each magnet-stator pair generates driving and levitation forces, we set

$$f_1 = f_{1x} i_x + f_{1z} i_z, \tag{6}$$

$$f_2 = f_{2y} i_y + f_{2z} i_z, \tag{7}$$

$$f_3 = f_{3x} i_x + f_{3z} i_z, \tag{8}$$

$$f_4 = f_{4y} i_y + f_{4z} i_z, \tag{9}$$

where i_x, i_y and i_z are the unit vectors.

Now, we define the displacement vectors from the center of mass of the platen to the centers of mass of each of four magnet arrays as $R_1 = [X_1 \quad Y_1 \quad Z_1]^T$, $R_2 = [X_2 \quad Y_2 \quad Z_2]^T$, $R_3 = [X_3 \quad Y_3 \quad Z_3]^T$ and $R_4 = [X_4 \quad Y_4 \quad Z_4]^T$. The values of the geometric parameters are $X_1 = X_4 = Y_3 = Y_4 = -112.8$ mm, $X_2 = X_3 = Y_1 = Y_2 = 90.4$ mm, and $Z_1 = Z_2 = Z_3 = Z_4 = -33.4$ mm in our levitator. We approximate the forces to act on the centers of the magnet arrays.

5.1. Linearized equations of motion

We follow the $x\,y\,z$ convention to define Euler angles, which is commonly used in engineering applications [13]. For small angular motions in our levitator, the Euler angles ψ, θ, and ϕ can be considered as rotational angles around x-, y-, and z-axes, respectively. We define twelve state variables to describe motions of the platen

$$[x\ y\ z\ u\ v\ w\ \psi\ \theta\ \phi\ p\ q\ r]^T. \tag{10}$$

The first six states are the position and velocity components of the center of the mass of the platen with respect to the origin of the inertial frame described in the inertial frame. The seventh, eighth, and ninth states are Euler angles. The last three states are the angular velocity components of the platen described in the body frame. We can show that the angular velocity components described in the inertial frame are approximately the same as those described in the body frame in case of small-angle linearized equations of motion.

Let us define $K_D = \frac{1}{2}\mu_0 M_0 \eta_0 N_m G e^{-\gamma_1 \bar{z}_0}$. Using the linearization equations for forces

$$\bar{f}_x = k_D \bar{i}_D \tilde{x} + k_D \tilde{i}_Q, \tag{11}$$

$$\bar{f}_y = k_D \bar{i}_D \tilde{y} + k_D \tilde{i}_Q , \tag{12}$$

$$\bar{f}_z = -k_D \gamma_1 \bar{i}_D \tilde{x} + k_D \tilde{i}_Q , \tag{13}$$

and the perturbation equations, the full state equations for small linear and angular position variations around the equilibrium point for the levitator can be shown by applying Newton's second law.

$$\dot{\tilde{x}} = \tilde{u} , \tag{14}$$

$$\dot{\tilde{y}} = \tilde{v} , \tag{15}$$

$$\dot{\tilde{z}} = \tilde{w} , \tag{16}$$

$$\dot{\tilde{u}} = \frac{1}{M} k_D (\bar{i}_{1D} + \bar{i}_{3D}) \tilde{x} + \frac{1}{M} k_D (\bar{i}_{1Q} + \bar{i}_{3Q}) , \tag{17}$$

$$\dot{\tilde{v}} = \frac{1}{M} k_D (\bar{i}_{2D} + \bar{i}_{4D}) \tilde{y} + \frac{1}{M} k_D (\bar{i}_{2Q} + \bar{i}_{4Q}) , \tag{18}$$

$$\begin{aligned} \dot{\tilde{w}} = & -\frac{1}{M} k_D \gamma_1 (\bar{i}_{1D} + \bar{i}_{2D} + \bar{i}_{3D} + \bar{i}_{4D}) \tilde{z} \\ & + \frac{1}{M} k_D (\bar{i}_{1D} + \bar{i}_{2D} + \bar{i}_{3D} + \bar{i}_{4D}), \end{aligned} \tag{19}$$

$$\dot{\tilde{\psi}} = \tilde{p} \tag{20}$$

$$\dot{\tilde{\theta}} = \tilde{q} \tag{21}$$

$$\dot{\tilde{\phi}} = \tilde{r} \tag{22}$$

$$\dot{\tilde{p}} = \dots$$

$$\dot{\tilde{q}} = \dots$$

$$\begin{aligned} \dot{\tilde{r}} = & I_{zx}^{-1} k_D (-Y_1^2 \gamma_1 \bar{i}_{1D} - Y_2^2 \gamma_1 \bar{i}_{2D} + Z_2^2 \bar{i}_{2D} \\ & - Y_3^2 \gamma_1 \bar{i}_{3D} - Y_4^2 \gamma_1 \bar{i}_{4D} + Z_4^2 \bar{i}_{4D}) \tilde{\psi} \\ & + I_{zy}^{-1} k_D (Z_1^2 \bar{i}_{1D} - X_1^2 \gamma_1 \bar{i}_{1D} - X_2^2 \gamma_1 \bar{i}_{2D} + Z_3^2 \bar{i}_{3D} \\ & - X_3^2 \gamma_1 \bar{i}_{3D} + X_4^2 \gamma_1 \bar{i}_{4D}) \tilde{\theta} \\ & + I_{zz}^{-1} k_D (Y_1^2 \bar{i}_{1D} + X_2^2 \bar{i}_{2D} + Y_3^2 \bar{i}_{3D} + X_4^2 \bar{i}_{4D}) \tilde{\phi} \\ & + k_D (I_{zy}^{-1} Z_1 - I_{zz}^{-1} Y_1) \tilde{i}_{1Q} + k_D (-I_{zx}^{-1} Z_2 + I_{zz}^{-1} X_2) \tilde{i}_{2Q} \\ & + k_D (I_{zy}^{-1} Z_3 - I_{zz}^{-1} Y_3) \tilde{i}_{3Q} + k_D (-I_{zx}^{-1} Z_4 + I_{zz}^{-1} Y_4) \tilde{i}_{4Q} \\ & + k_D (I_{zx}^{-1} Y_1 - I_{zy}^{-1} X_1) \tilde{i}_{1D} + k_D (I_{zx}^{-1} Y_2 - I_{zy}^{-1} X_2) \tilde{i}_{2D} \\ & + k_D (I_{zx}^{-1} Y_3 - I_{zy}^{-1} X_3) \tilde{i}_{3D} + k_D (I_{zx}^{-1} Y_4 - I_{zy}^{-1} X_4) \tilde{i}_{4D}. \end{aligned} \tag{23}$$

The expressions for $\dot{\tilde{p}}$ and $\dot{\tilde{q}}$ are similar to the expression for $\dot{\tilde{r}}$ and are omitted for the sake of brevity. The inertia tensor is represented by a 3×3 matrix

$$\begin{aligned} I &= \begin{bmatrix} I_{xx} & -I_{xy} & -I_{xz} \\ -I_{yx} & I_{yy} & -I_{yz} \\ -I_{zx} & -I_{zy} & I_{zz} \end{bmatrix} \\ &= \begin{bmatrix} 0.0541 & 0.00276 & -0.00253 \\ 0.00276 & 0.0541 & -0.00261 \\ -0.00253 & -0.00261 & 0.0981 \end{bmatrix} \end{aligned} \tag{24}$$

in kg-m^2. This completes the derivation of the state-space equations of motion of the stage.

If we neglect coupling terms between the vertical and horizontal modes, the linearized small-signal lateral mode dynamics can be represented as follows by substituting parameters given above [2].

$$\begin{aligned} \begin{bmatrix} \dot{\tilde{x}} \\ \dot{\tilde{y}} \\ \dot{\tilde{\phi}} \\ \dot{\tilde{u}} \\ \dot{\tilde{v}} \\ \dot{\tilde{r}} \end{bmatrix} &= \begin{bmatrix} 0 & 0 & 0 & 1 & 0 & 0 \\ 0 & 0 & 0 & 0 & 1 & 0 \\ 0 & 0 & 0 & 0 & 0 & 1 \\ 4.9672 & 0 & 0 & 0 & 0 & 0 \\ 0 & 4.9672 & 0 & 0 & 0 & 0 \\ 0 & 0 & 5.8440 & 0 & 0 & 0 \end{bmatrix} \begin{bmatrix} \tilde{x} \\ \tilde{y} \\ \tilde{\phi} \\ \tilde{u} \\ \tilde{v} \\ \tilde{r} \end{bmatrix} \\ &+ \begin{bmatrix} 0 & 0 & 0 & 0 \\ 0 & 0 & 0 & 0 \\ 0 & 0 & 0 & 0 \\ 4.9672 & 0 & 4.9672 & 0 \\ 0 & 4.9672 & 0 & 4.9672 \\ -26.0235 & 26.0092 & 31.4955 & -31.5107 \end{bmatrix} \begin{bmatrix} \tilde{i}_{1Q} \\ \tilde{i}_{2Q} \\ \tilde{i}_{3Q} \\ \tilde{i}_{4Q} \end{bmatrix} \end{aligned} \tag{25}$$

The open-loop poles are at ±2.2287, ±2.2287 and ±2.4174 rad/s. The plant model for the lateral mode is unstable, and the instability comes from the negative springs from the electromagnetic origin.

5.2. Linear quadratic regulation for lateral modes

We represent the above dynamic system as follows.

$$\dot{x}(t) = Ax(t) + Bu(t) \tag{26}$$

where x is the state vector and u is the input vector. Define the performance index

$$V(x(t_0), u(\cdot),\ t_0) = \int_{t_0}^{\infty} (u^T(t) R u(t) + x^T(t) Q x(t))\ dt. \tag{27}$$

The time-invariant infinite-time regulator problem is a minimization problem to find an optimal control u^* to minimize V. The solution of this problem is well-known and can be found in texts on optimal control such as [6]. As minimizing the errors in the position state variables is one of the most important control objectives, much greater penalties were assigned for these variables. On the other hand, the same amount of penalties was assigned for each of the inputs. We found an optimal controller associated with the performance index defined above using $Q = \mathrm{diag}(10000\ 10000\ 10000\ 10\ 10\ 10)$ and $R = \mathrm{diag}(1\ 1\ 1)$,

The corresponding closed-loop system $\dot{x}(t) = (A - BR^{-1}B^T P)x(t)$ is

The closed-loop poles are placed at −179.92, −32.12, −21.84 ± j15.01, and −21.78 ± j15.00 rad/s, so the closed-loop system has been stabilized. As the controller is to be implemented digitally in a 320C40

$$\begin{bmatrix} \dot{\tilde{x}} \\ \dot{\tilde{y}} \\ \dot{\tilde{\phi}} \\ \dot{\tilde{u}} \\ \dot{\tilde{v}} \\ \dot{\tilde{r}} \end{bmatrix} = \begin{bmatrix} 0 & 0 & 0 & 1 & 0 & 0 \\ 0 & 0 & 0 & 0 & 1 & 0 \\ 0 & 0 & 0 & 0 & 0 & 1 \\ -701.23 & -1.2623 & -41.961 & -43.633 & -0.051255 & -1.3918 \\ -1.2623 & -701.22 & 42.188 & -0.051255 & -43.632 & 1.3993 \\ -41.948 & 42.175 & -5777.8 & -1.3905 & 1.3980 & -212.01 \end{bmatrix} \begin{bmatrix} \tilde{x} \\ \tilde{y} \\ \tilde{\phi} \\ \tilde{u} \\ \tilde{v} \\ \tilde{r} \end{bmatrix}$$

$$\begin{bmatrix} \tilde{i}_{1Q} \\ \tilde{i}_{2Q} \\ \tilde{i}_{3Q} \\ \tilde{i}_{4Q} \end{bmatrix}^* = -\begin{bmatrix} 74.0904 & -2.8995 & -45.6450 & 4.5886 & -0.1925 & -1.6894 \\ -2.8833 & 74.1054 & 45.6230 & -0.1914 & 4.5897 & 1.6887 \\ 68.0698 & 3.1536 & 54.0928 & 4.1955 & 0.2028 & 1.9696 \\ 3.1374 & 68.0522 & -54.1164 & 0.2017 & 4.1944 & -1.9704 \end{bmatrix} \begin{bmatrix} \tilde{x} \\ \tilde{y} \\ \tilde{\phi} \\ \tilde{u} \\ \tilde{v} \\ \tilde{r} \end{bmatrix} \tag{29}$$

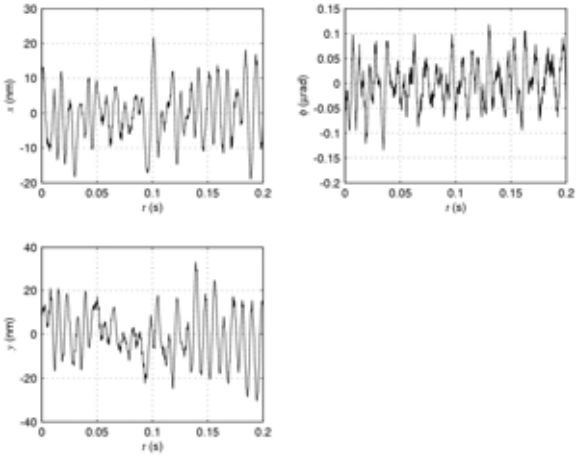

Fig. 9. Position regulation with a linear quadratic regulator for the lateral dynamics.

digital signal processor, we need the control gain in the discrete-time domain. The discrete-time feedback gain is calculated with the 'lqrd' function in MATLAB. The 'lqrd' function discretizes the continuous plant and continuous cost function weighting matrices using the sample time and the zero order hold approximation [14]. The sampling of the controller is 5 kHz. Fig. 9 shows the lateral position regulation results by the linear quadratic rate rate regulator designed above. The position noise in the x and y axes is with a 40-nm envelope. The position noise in ϕ is 0.15 μrad.

5.3. Time-optimal control

In the previous section, we discussed the design and implementation of an LQ regulator to regulate the position of the platen. Besides the position regulation, fast motion generation is another important control objective to enhance the machine throughput as semiconductor manufacturing equipment. We formulate a time-optimal control problem without penalty in the control efforts as follows.

Find a control u for the plant

$$\dot{x}(t) = Ax(t) + Bu(t), \tag{30}$$

which minimize the performance index

$$V(x(t_0), u(\cdot),\ t_0) = \int_{t_0}^{\infty} (x^T(t) Q x(t))\ dt. \tag{28}$$

with the inequality constraint,

$$|u| \le 1. \tag{32}$$

The solution of this singular optimal control is known as the bang-bang mode control [6]. In a practical system under the influence of disturbance and noise, chattering is a significant problem especially at the end of the trajectory. This problem was solved with dual mode of sliding mode control [6] or proximate time optimal control [15].

Many practical systems frequently have limitations on the amount of control effort. Taking our levitation system for example, we designed the maximum phase current of the linear motors as 1.5 A. In many real systems, however, there are other constraints along with this actuator constraint. In high-precision motion control system as ours employing laser interferometer system, the laser head slew rate constraint proves to be much more binding constraints. The laser head (HP5517B) has the maximum velocity rating at 254 mm/s for a plane mirror measurement system. If we accelerate the platen at 12.5 m/s^2, it takes only 20-ms to reach 250 mm/s velocity at this acceleration and the displacement is 5 mm at t = 20 ms. We could use the bang-bang control for 20-mm steps, but the velocity of the platen would be out of range because of the slew rate constraint of the laser head.

For the fastest motion control, we accelerate the platen at the highest acceleration possible until the velocity reaches the slew rate, then decelerate the platen at the same acceleration to brake the platen motion.

Fig. 10 shows test results with repetitive 20-mm steps

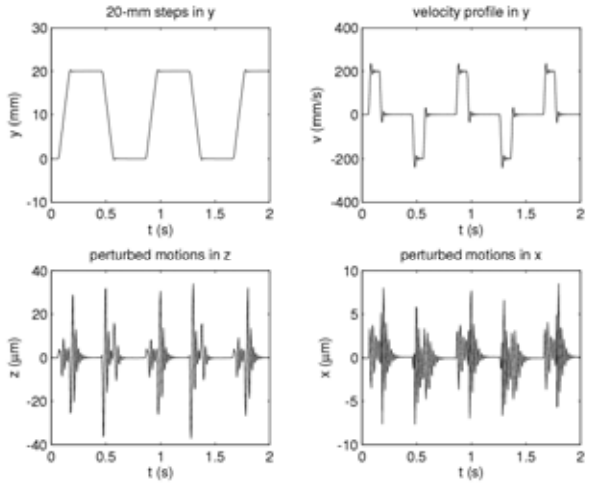

Fig. 10. 20-mm repetitive steps in y following the time-optimal path.

in y direction. The acceleration given to the platen is 20 m/s^2 (about 2-g) and the platen maintains 200-mm/s velocity in the middle sections of the contour. It takes only 110 ms to complete a 20-mm step. This fast response confirms the utility of the magnetic levitation technology in fast high-precision active motion control applications.

Testing results also show small perturbed motions in z and ϕ. However, they guarantee that there is no collision between the platen and the stators at any instance of time since the zero point for z of the platen is set at 450-μm air gap. The error motions in the other axes depict the coupling nature of the platen dynamics. We could not operate the platen at the maximum velocity rating (254 mm/s) due to the velocity ringing at the beginning and the end of the step motions.

6. CONCLUSIONS

In this paper, we presented the recent theoretical and experimental developments in the planar magnetic levitator. Using a stochastic system identification methodology, the first resonant frequency of the platen was shown as high as 750 Hz. This confirmed the effectiveness of the aluminum honeycomb composite structure for its high stiffness-to-mass ratio. This high structural resonant frequency enabled us to implement a controller with a 100-Hz crossover frequency. This high-bandwidth controller led to fast platen dynamics; the platen now follows a 20-mm step command in 110 ms, and possesses 2-g acceleration (20 m/s^2) capability. With noise/disturbance modeling and analysis, we have shown that the positioning noise covariance of the current maglev system can be decreased by morehan a factor of 100 with better metrology and environment control.

Adequate metrology is essential to improve the current planar magnetic levitator's performance. Position resolution and positioning noise can be enhanced by multi-axis high-resolution laser interferometry with multiple-path optics. Error corrections such as surface mapping of mirrors, and corrections of wave length variation due to temperature, humidity, and air density are also required. Along with metrology, the operation environment becomes significant for next-generation precision instrument/manufacturing equipment. First, since the dimensional stability of the metrology devices is very sensitive to the temperature variation, maintaining the operational temperature within tens of milli-Kelvin will be required. Second, the vibration isolation system should be optimized to provide adequate damping and stiffness as well as low floor-vibration transmissibility. To facilitate settling of the stage in a tight nanometer position window, an active vibration isolation system can damp table motions due to reaction forces besides rejecting floor vibration.

Since the single-moving platen generates all 6-DOF motions, and its dynamics is coupled among its axes, multivariable modeling and control is required to represent the planar magnetic levitator dynamics with fidelity. To regulate the positioning error, we designed and implemented a multivariable linear quadratic regulator for lateral dynamics of the magnetic levitator. The design was based on the analytical work published previously by the author [3]. The x- and y-positioning noise of the lateral modes is on the order of 40-nm. This regulator stabilizes the inherently unstable lateral modes of the levitator and has a good stability margin.

We also provided test results on the time-optimal control of the maglev stage. Fast responses and effective command tracking are very important in semiconductor manufacturing applications, since they are directly related to the machine throughput. The magnetic levitator's dynamic performance is limited by the finite slew rate of the laser head. We modified the result in time-optimal control, and demonstrated that the stage could complete a 20-mm step only in 110 ms at maximum 2g acceleration. Perturbed motions in other axes were maintained within reasonable bounds for safe operation.

Magnetic levitation is an enabling technology in the high-precision active planar motion control field. In the future deep-submicron technology, fast and precise motion control of material handling equipment is highly required. We demonstrated the utility of the maglev technology in high-precision planar positioning applications.

REFERENCES

[1] W.-J. Kim and D. L. Trumper, "High-precision magnetic levitation stage for photolithography," *Precision Engineering*, vol. 22, no. 2, pp. 66-77, April 1998.

[2] W.-J. Kim, *High-Precision Planar Magnetic Levitation*, Ph.D. Thesis, Department of Electrical Engineering and Computer Science, Massachusetts Institute of Technology, June 1997.
[3] D. L. Trumper, W.-J. Kim, and M. E. Williams, "Design and analysis framework for linear permanent-magnet machines," *IEEE Trans. on Industry Applications*, vol. 3, no. 2, pp. 371-379, March/April 1996.
[4] K. G. Shin and N. D. McKay, "Minimum-time control of robotic manipulators with geometric path constraints," *IEEE Trans. on Automatic Control*, vol. 30, no. 6, pp. 531-541, June 1985.
[5] J.-J. E. Slotine and H. S. Yang, "Improving the efficiency of time-optimal path-following algorithms," *IEEE Trans. on Robotics and Automation*, vol. 5, no. 1, pp. 118-124, February 1989.
[6] B. D. O. Anderson and J. B. Moore, *Linear Optimal Control*, Prentice-Hall, Inc., 1971.
[7] K. Halbach, "Design of permanent multipole magnets with oriented rare earth cobalt material," *Nuclear Instruments and Methods*, vol. 169, no. 1, pp. 1-10, 1980.
[8] P. S. Maybeck, *Stochastic Models, Estimation, and Control*, Academic Press, 1979.
[9] L. Ljung and T. Soderstrom, *Theory and Practice of Recursive Identification*, MIT Press, 1983.
[10] S. J. Ludwick, *Modeling and Control of a Six Degree of Freedom Magnetic/Fluidic Motion Control Stage*, Master's Thesis, Massachusetts Institute of Technology, February 1996.
[11] A. Blondel, *Synchronous Motor and Converters*, McGraw-Hill Book Co., 1913.
[12] R. H. Park, "Two-reaction theory of synchronous machines, generalized method of analysis-Part I" *Transactions AIEE*, vol. 48, no. 3, pp. 716-730, 1929.
[13] H. Goldstein, *Classical Mechanics*, Addison-Wesley Publishing Co., Inc., 1980.
[14] Mathworks, Inc., *Control Systems Toolbox for Use with MATLAB*, 1992.
[15] M. L. Workman, R. L. Kosut, and G. F. Franklin, "Adaptive proximate time-optimal control: Continuous time case," *Proc. of the Automatic Control Conference*, pp. 589-594, 1987.

Won-jong Kim received the B.S. (summa cum laude) and M.S. degrees in Control and Instrumentation Engineering from Seoul National University, Seoul, Korea, in 1989 and 1991, respectively, and the Ph.D. degree in Electrical Engineering and Computer science from Massachusetts Institute of Technology, Cambridge, in 1997.

In September 2000, he joined the Department of Mechanical Engineering, Texas A&M University, where he is currently an Assistant Professor. Following receipt of the PhD degree, he was with SatCon Technology Corporation in Cambridge, Massachusetts, for three years. His teaching and research interests focus on analysis, design, and real-time control of mechatronic systems, and nanoscale engineering and technology.

He received the Grand Prize from the Korean Institute of Electrical Engineers' Student Paper Contest in 1988, and the Gold Prize for his doctoral work from Samsung Electronics' Humantech Thesis Prize in 1997. He was a semifinalist of the National Institute of Standards and Technology's Advanced Technology Program 2000 Competition. The National Aeronautics and Space Administration granted him the Space Act Award for his contributions in the development of an extended-range magnetostrictive actuator for robotic applications in July 2002